

Local effects of biased electrodes in the divertor of NSTX

This article has been downloaded from IOPscience. Please scroll down to see the full text article.

2012 Plasma Phys. Control. Fusion 54 105012

(<http://iopscience.iop.org/0741-3335/54/10/105012>)

View [the table of contents for this issue](#), or go to the [journal homepage](#) for more

Download details:

IP Address: 198.125.228.208

The article was downloaded on 05/09/2012 at 20:42

Please note that [terms and conditions apply](#).

Local effects of biased electrodes in the divertor of NSTX

S J Zweben, M D Campanell, B C Lyons, R J Maqueda, Y Raitses, A L Roquemore, F Scotti and H Takahashi

Princeton Plasma Physics Laboratory, Princeton, NJ 08540, USA

Received 8 May 2012, in final form 9 August 2012

Published 5 September 2012

Online at stacks.iop.org/PPCF/54/105012

Abstract

The goal of this paper is to characterize the effects of small non-axisymmetric divertor plate electrodes on the local scrape-off layer plasma. Four small rectangular electrodes were installed into the outer divertor plates of NSTX. When the electrodes were located near the outer divertor strike point and biased positively, there was an increase in the nearby probe currents and probe potentials and an increase in the Li I light emission at the large major radius end of these electrodes. When an electrode located farther outward from the outer divertor strike point was biased positively, there was sometimes a significant decrease in the Li I light emission at the small major radius end of this electrode, but there were no clear effects on the nearby probes. No non-local effects were observed with the biasing of these electrodes.

(Some figures may appear in colour only in the online journal)

1. Introduction

A large fraction of the plasma energy leaving the edge of a tokamak will go onto the divertor plate surfaces just outside the magnetic separatrix. This ‘scrape-off layer’ (SOL) heat flux will be up to $\sim 10 \text{ MW m}^{-2}$ at the divertor plates of ITER [1], which is uncomfortably close to the limit of heat removal technology. In addition, the large particle flux will eventually erode or damage these surfaces, requiring routine replacement.

One proposed solution to these problems is to generate non-axisymmetric convective cells just above the divertor plates in order to spread the heat and particle flux over a wider radial area [2–4]. The simplest way to create such convective cells would be to electrically bias isolated segments of the divertor plate to form a local peak in the electrostatic potential. The resulting convective $v_{E \times B}$ plasma motion around the B -field lines should move the heat or particle flux radially inward or outward, depending on the direction of $v_{E \times B}$ with respect to the local major radius. Convective cells near the divertor plates might also be generated by non-axisymmetric variations in the divertor surface height, the surface material, or cold gas influx [2]. Note that any magnetic perturbations due to the current drawn by these electrodes are not relevant for this convective cell effect, although recently the magnetic effects of the SOL currents from similar electrodes were also evaluated as a method for ELM control [5].

A schematic view of convective cell generation is shown in figure 1. A small circular electrode on the divertor plate is shown as the coin-shaped object at the right. The incoming

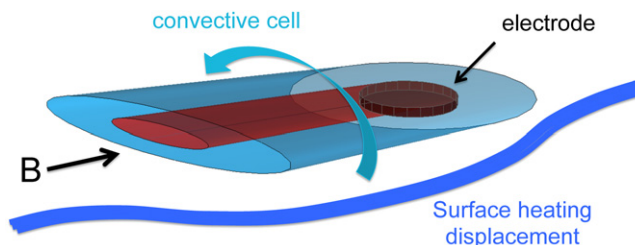


Figure 1. Schematic illustration of a local convective cell generated by a non-axisymmetric divertor plate electrode. The inner (red) tube shows a magnetic flux tube connected to a circular electrode (black disk), where the magnetic field line intersects the electrode at a small angle ($\sim 15^\circ$). The outer (blue) tube shows a larger convective cell created by potentials leaking outside the electrode flux tube. The convective motion could in principle displace the location of the heat and particle flux hitting the divertor plate as indicated.

magnetic field intercepts this electrode at a shallow angle, and the flux tube connected to the electrode is shown as the smaller flattened tube. If biasing creates a local peak in the electrostatic potential inside this tube, then the plasma inside this tube will rotate in a convective cell around the B -field line. If the electrostatic potential extends farther across B it could create a larger convective cell, as shown by the larger flattened tube. This larger convective cell could cause a radial displacement of the heat and particle flux hitting the divertor surface near the electrodes, as indicated by the deflected line. The amount of displacement will depend on the 3D structure of these electrostatic potentials, and also on the competing plasma transport

mechanisms. The goal of this experiment is to observe any such local effects due to electrode biasing in NSTX.

There have been many previous experiments on plasma biasing in toroidal fusion devices over the past 30 years, for example [6–17]. However, most of these aimed to create *axisymmetric* radial or poloidal electric fields in the plasma edge using electrodes or large-area wall biasing to control the edge plasma transport. Many of these experiments reported changes in the edge turbulence due to edge biasing, and a lowered threshold for the H-mode transition. These effects are very interesting and potentially important, but are not the focus of this paper since axisymmetric potentials will not create local convective cells.

This work aimed to create *local non-axisymmetric* electric fields to cause local changes in the heat and particle flux to the wall. Evidence for convective cell formation induced by non-axisymmetric biased electrodes was previously obtained in JFT-2M [11], CASTOR [15] and MAST [18]. A prior experiment on NSTX also evaluated the effects of a pair of small biased electrodes inserted into the SOL just below the outer midplane limiter [19]. In that case clear evidence for convective cell formation was inferred from variations in the measured radial profile of density between those electrodes. Note that *positive* electrode biasing was advocated to create such a convective cell in theory [2–4], and only positive biasing had any effect in the previous NSTX experiments [19]. For negative biasing the potential drop across the sheath is large and so significantly reduces the potential available for the convective cell formation.

Very recently, the creation of convective cells was studied in a simple magnetized torus TORPEX using a 2D array of positively biased electrodes at the outer midplane [20, 21]. These convective cells were generated in a configuration similar to midplane experiments in NSTX, and caused a significant deflection of the turbulent blob motion in their vicinity. The created potentials were fairly uniform along the magnetic field, but there was also evidence for significant cross-field currents, and for a shift in the potential structure due to plasma rotation.

The goal of this paper is to evaluate the local effects of the biased divertor electrodes. The electrode geometry and diagnostics are described in section 2, and the experimental results are described in section 3. Section 4 contains a summary, some discussion of modeling, and the conclusions.

2. Electrodes, diagnostics and database

This section describes the electrodes, the diagnostics, and the database used for this experiment. The local effects of the electrode biasing were measured using Langmuir probes and a visible light camera viewing the electrodes from above. The database consisted of five run days of NSTX operation in 2010.

2.1. Electrodes

Photos of the divertor electrodes used for these experiments are shown in figure 2. There were two different pairs of rectangular electrodes located in the outboard divertor plates at the floor

of NSTX about 180° apart from each other in the toroidal direction. One pair was oriented in the toroidal direction (left side of figure 2), and one pair oriented in the radial direction (right side of figure 2).

The radial electrodes were 3.8 cm long and 1.2 cm wide, extending over the major radial region $R = 76.2\text{--}80.0$ cm, with a toroidal spacing between the electrodes of 1.2 cm. The toroidal electrodes were 4.0 cm long and 1.1 cm wide, centered at $R = 76.9$ cm and $R = 80.5$ cm with a radial spacing between electrodes of 2.5 cm. There was a $\sim 1\text{--}2$ mm vacuum gap ~ 1 cm deep between the electrodes and the surrounding tile (which was at ground potential), in order to minimize the effects of coatings and arcing. The electrodes and local tiles were made of ATJ graphite. The top surfaces of the electrodes were nearly flush with the local tiles, and the bottom surfaces of the electrodes were mounted on a boron nitride holder. An effort was made to maximize the thermal coupling between the electrodes and their boron nitride holders in order to limit the temperature rise. Tests outside the vessel (performed in air) showed that a heated electrode thermalized with the adjacent divertor tile in 40 s, so the electrodes should cool between shots 10 min apart.

The electrode power supplies were the same as used previously for the NSTX midplane electrode experiments [19]. For positive biasing there were two 100 V, 30 A dc supplies which could be turned on and off at any time during the discharge. With ‘bias on’ the electrode potential was applied with respect to the vacuum vessel ground, and with ‘bias off’ the electrodes were floating with respect to the vessel. The electrodes were always modulated at 50 Hz so the ‘bias on’ effects could be compared with the ‘bias off’ every 20 ms. The voltages and currents were monitored at 20 kHz at the power supply.

2.2. Langmuir probes

The Langmuir probe arrays are also shown in the photos of figure 2. There were five probes in a radial array near each pair of electrodes, labeled R1–R5 for the radial electrodes and T1–T5 for the toroidal electrodes. The probes were vertical cylinders 0.16 cm in diameter, mounted flush or slightly below the surrounding tiles. There was a ~ 1 mm vacuum gap ~ 1 cm deep between the probes and the surrounding tile (which was at ground potential), in order to minimize the effects of coatings and arcing.

The radial separation between each of the probes was 1.5 cm, and the probes extended from $R = 75.3\text{--}81.1$ cm for the radial electrodes and $R = 75.8\text{--}81.7$ cm for the toroidal electrodes. The toroidal distances between the probes and the radial electrode edge were 1.4 cm, and 2.2 cm for the radial and toroidal electrodes, respectively. The magnetic field direction indicated in figure 2 is such that the magnetic flux tubes from the plasma passed over the nearby probes before intersecting the electrodes.

The density and temperature inferred from these probes were roughly $n \sim (5\text{--}10) \times 10^{12} \text{ cm}^{-3}$ and $T_e \sim 10\text{--}20$ eV (see section 4.4). However, since the exact depth of the probe tips below the local tile surfaces varied between ~ 0.5 and 1 mm from probe to probe, and since their surface conditions evolved

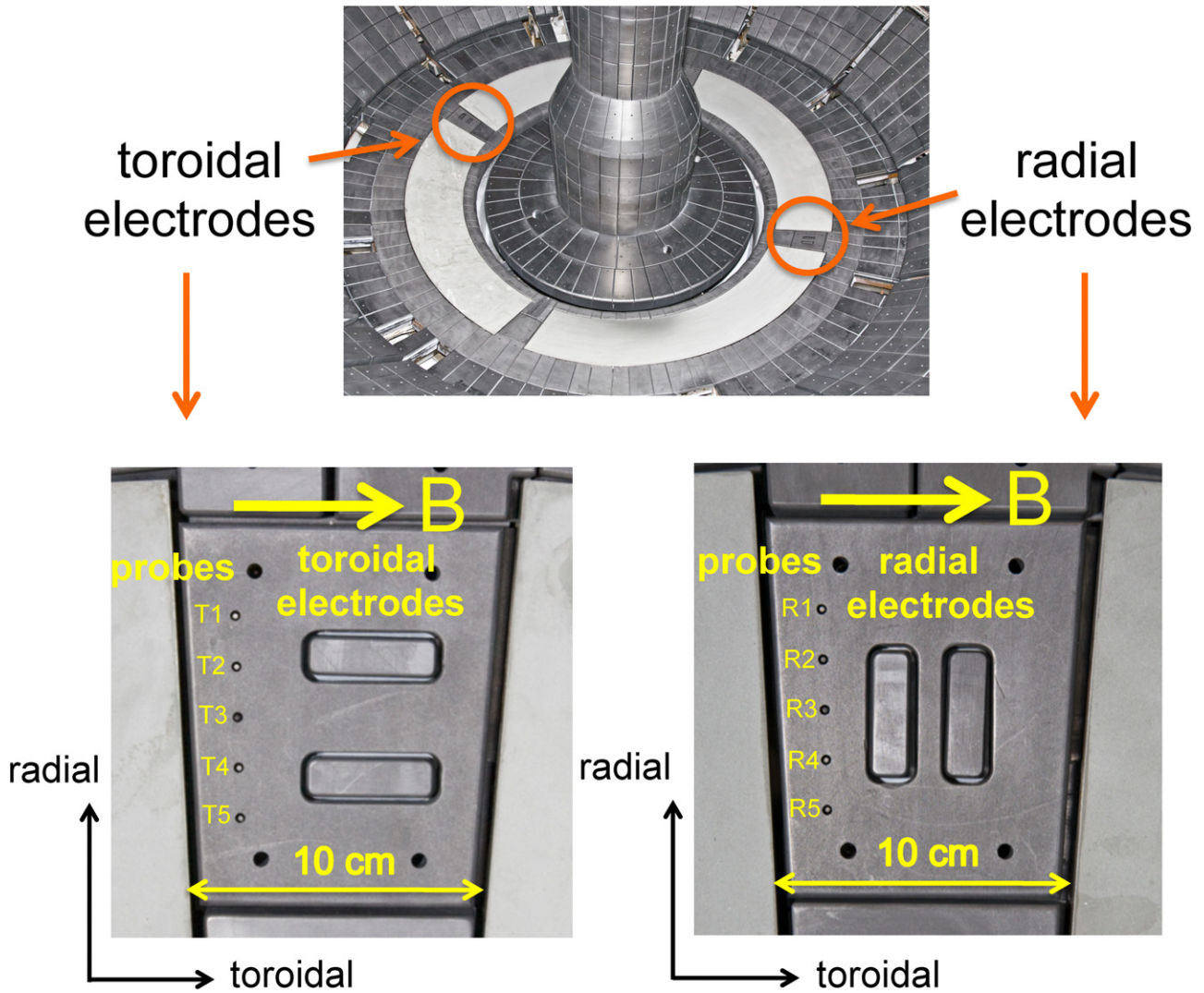


Figure 2. Photos of the electrodes and probes in this experiment. At the bottom right are the radially oriented electrodes, and at the bottom left are the toroidal-oriented electrodes, which are located 180° apart from each other on the divertor floor of NSTX. Next to each pair of electrodes is a radial array of five Langmuir probes. The electrodes are each ~4 cm × 1 cm in area, and the probes are ~0.16 cm in diameter. In the bottom photos the outward major radial direction is upward, the toroidal direction is horizontal, and the local plasma flows along B from left to right on its way toward the electrodes.

differently over time due to erosion or deposition, the probes are not very reliable for making absolute density measurements or for radial profiles of the density or temperature. They were used mainly to measure relative changes in probe current and floating potential due to electrode biasing.

The Langmuir probe power supply was the same as used for previous midplane biasing experiments [19]. The probes were driven by a single supply which provided up to ±50 V dc. This voltage could also be swept over this range, or disconnected from the supply to measure the floating potential to ground. The probe currents were monitored using a 50 Ω series resistor, and five probe voltage and current signals were digitized at 200 kHz for each shot.

2.3. Cameras

Since the spatial resolution of the Langmuir probes was very limited, the effects of electrode biasing were also monitored

using high-speed cameras to view the electrode regions during these runs. These cameras were mounted at the top of NSTX about 2 m above the divertor floor, and viewed the electrodes through the plasma. Both cameras had remotely controlled optical filters which could be changed from shot-to-shot. The filters used here were Li I (670.8 nm), D_α (656 nm) and IR (~900–1100 nm). The image magnification could be changed from day-to-day with different camera lenses. More information about the camera hardware and operation can be found in [22].

Most of the camera results in section 4 were obtained using Li I filters, since NSTX had a substantial coating of evaporated lithium on the divertor plates during these runs, and so the deuterium recycling level was relatively low. Since the first ionization potential of lithium is only ~5 eV, it is very likely that the observed Li I light comes from a thin layer very close to the surface of the lithium source at the divertor plate. Previous measurements of moving edge turbulence filaments at the divertor

surface were made in Li I light using these cameras, and the Li I light fluctuations near the divertor plate were well correlated with midplane ‘blobs’ [23], suggesting that the Li I light was responding to electron density fluctuations, as it should.

However, the level of Li I light emission also depends on the electron temperature and on the local neutral lithium density, which depends on the incident ion sputtering and the surface evaporation rate. Therefore we cannot assume a simple linear relationship between the Li I light level and the local electron density, and so use the Li I light only as a qualitative indication of where in space and time the electrodes were changing the local plasma.

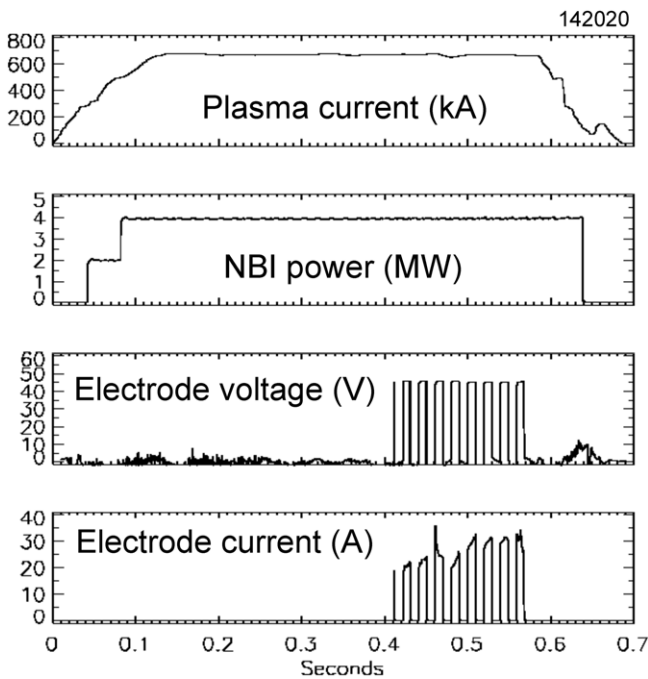


Figure 3. Typical time dependence of the electrode voltages and currents with respect to the plasma current and NBI injected power. The electrode voltages were typically +50–90 V and drew currents of ≤ 30 A per electrode, and were modulated at 50 Hz. These experiments had either NBI or RF heating and a wide range of plasma currents and fields.

2.4. Database

Figure 3 shows the way in which the electrode biasing was applied for 5–20 successive modulation cycles during the plasma current flat-top period for each shot in the database. Each modulation cycle consisted of 10 ms with the biasing on followed by 10 ms with the biasing off. A total of 47 shots were made with at least one of the electrodes biased positively from +50–90 V, as shown in table 1. Negative biasing was not used often due to previous results on NSTX showing no effects [19]. Each run in table 1 was performed on a different day with a different set of electrodes. The ‘N bias’ row in table 1 is the number of electrodes which were positively biased near the monitored probes, and the rows labeled ‘V bias’ and ‘I bias’ are the average electrode voltages and current for each electrode for that run.

The plasma conditions varied considerably over this database, with a range of plasma current 300–1000 kA, a range of auxiliary heating power 0–5 MW NBI and 0–1.3 MW RF, which included both L-mode and H-mode plasmas. These variable parameters resulted in a wide range of electrode currents in the range ~ 1 –30 A per electrode, depending on the plasma density and the proximity of the OSP to the electrodes.

3. Experimental results

Sections 3.1 and 3.2 describe in detail the results from the Langmuir probes and cameras for two of the five runs of table #1. Section 3.1 discusses the run which showed the biggest effects near the radial electrodes, and section 3.2 describes the run which had a magnified camera view of a toroidal electrode. A summary of the probe results from the other runs is presented in section 3.3, and the absence of other non-local effects is discussed in section 3.4.

An important variable in these experiments was the ‘outer strike point’ (OSP) location, which is the major radius of the peak heat and particle flux striking the outer divertor plate. In section 3.1 the OSP is identified by the bright toroidal band of Li I light emission seen in the camera view of the above. In section 3.2 this strike point was outside the camera field of view, and so was identified by the outer magnetic separatrix

Table 1. NSTX runs with electrode biasing.

	Run				
	#1	#2	#3	#4	#5
Electrodes	Radial	Toroidal	Toroidal	Radial	Toroidal
Shots	140333-347	140617-630	141839-899	142014-026	142490-507
I (kA)	300–650	900	640–1000	650–740	800–900
B (kG)	5.4–5.5	4.7	5.4	5.0–5.4	4.7
NBI (MW)	0–2	1.9–3.0	0–2	2–4	4
RF (MW)	0–1.5	0	0–1.3	0	0
OSP (cm)	40–70	62–75	40–79	76–80	72–75
Shots	11	4	19	6	7
Cycles	61	73	109	43	34
N + bias	1	1	2	2	2
V bias(V)	90	90	90	50	50–90
I bias(A)	1.0	9.6	2.3	24.5	19
Effect	None	Small	None	Large	Moderate

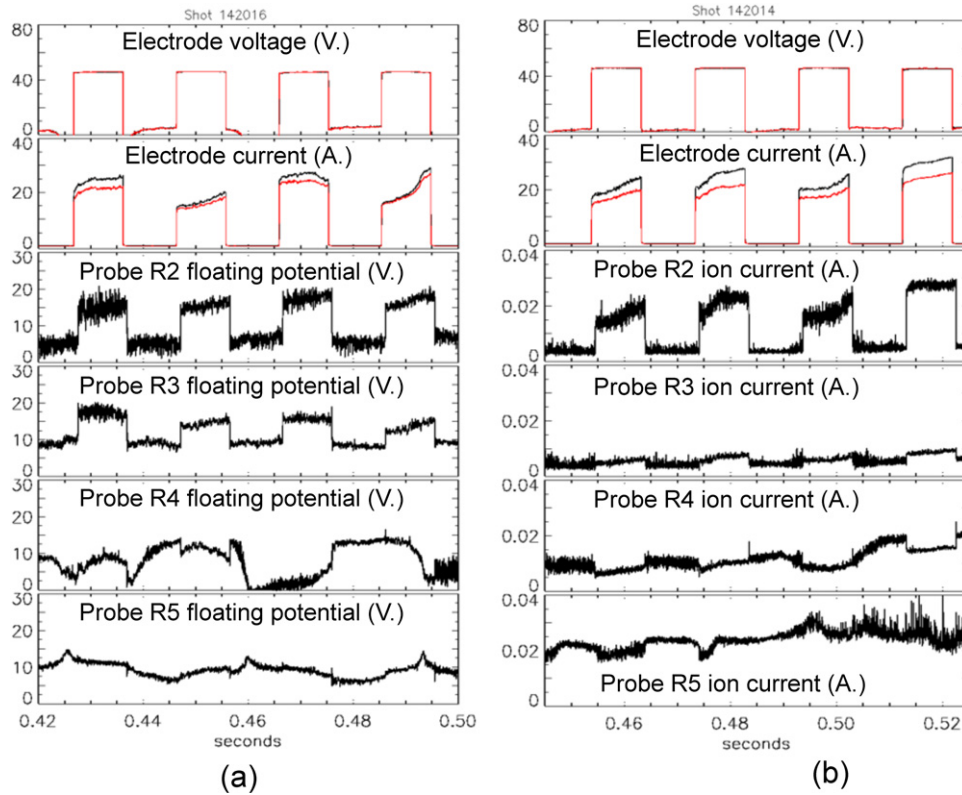


Figure 4. Electrode and probe signals versus time for typical shots with biasing of the radial electrodes (run #4). The electrode voltages and currents are shown at the top. Both of the electrodes are positively biased at +50 V in these shots and draw ~ 20 –30 A each. The probe floating potentials are shown at the left, and the probe ion saturation currents are shown at the right (for a -50 V probe bias). The probes labeled R2–R5 correspond to the locations shown at the right of figure 2. At the largest major radii R2 and R3 there was a prompt increase in the probe floating potential and current with biasing.

location at the divertor plate (as determined by EFIT). For cases in which both methods for identifying the OSP were available, the magnetic OSP was ~ 1 –3 cm radially outside the Li I light band, similar to a result for Langmuir probe signals in NSTX [24]. Therefore the magnetic OSP location should be considered uncertain by ~ 1 –3 cm in these experiments.

3.1. Radial electrodes near OSP

This section describes the cases which showed the largest local effects due to electrode biasing, in which both radial electrodes were biased at +50 V and together drew a relatively large total current of ~ 50 A. These were H-mode plasmas from run #4 (see table 1) with $B = 5.2 \pm 0.2$ kG, $I = 700 \pm 50$ kA, $P_{\text{NBI}} = 4$ –5 MW, $T_e(0) = 0.9$ keV and $n(0) = 7 \times 10^{13}$ cm $^{-3}$.

Figure 3 showed an example of the time dependence of the plasma current and NBI power and electrode voltage and current. The biasing was turned on at ~ 0.4 s and was modulated at 50 Hz for about 150 ms. The slow increase in electrode current over time is most likely associated with the slow increase in plasma density over this time.

3.1.1. Effects in the nearby Langmuir probes. Figure 4 shows typical electrode and probe signals versus time for two shots in this run. For the shot in figure 4(a) the nearby Langmuir probes were floating, and for the shot in figure 4(b) the nearby probes were biased at -50 V. The top row shows the electrode

voltages, which were +50 V during biasing and near zero with no biasing when the electrodes were floating. The second row shows the electrode currents, which were in the range 15–30 A for each electrode during this time (the electrode with slightly higher current is the one nearer to the probes).

The next two rows of figure 4(a) show the floating potentials in probes R2 and R3 near the large major radius end of the electrode, which clearly increase by ~ 5 –10 V within 1 ms of the bias turn-on, and then drop back to their pre-bias levels within 1 ms when the bias is turned off. The floating potential in probe R4 at the small major radius edge of the electrode sometimes increased and sometimes decreased with electrode biasing, while probe R5 about 1 cm inboard of the electrode edge showed little or no systematic change with biasing. In figure 4(b) the ion saturation currents in probes R2 and R3 increased by up to a factor of 3–5 within 1 ms of the electrode biasing, and then dropped back to their pre-bias levels within 1 ms after the biasing was turned off. Probe R4 at the bottom edge of the electrode shows a small *decrease* in ion saturation current with electrode biasing, while probe R5 below the electrode shows little or no response to the biasing. Probe R1 was not available for these shots.

Figure 5 shows average effects of electrode biasing on these probes for 43 bias on-off cycles for this run. For figure 5(a) the floating potentials for each probe were averaged over the middle 5 ms of every ‘bias on’ half-cycle and for the following ‘bias off’ half-cycle, and these potential profiles are

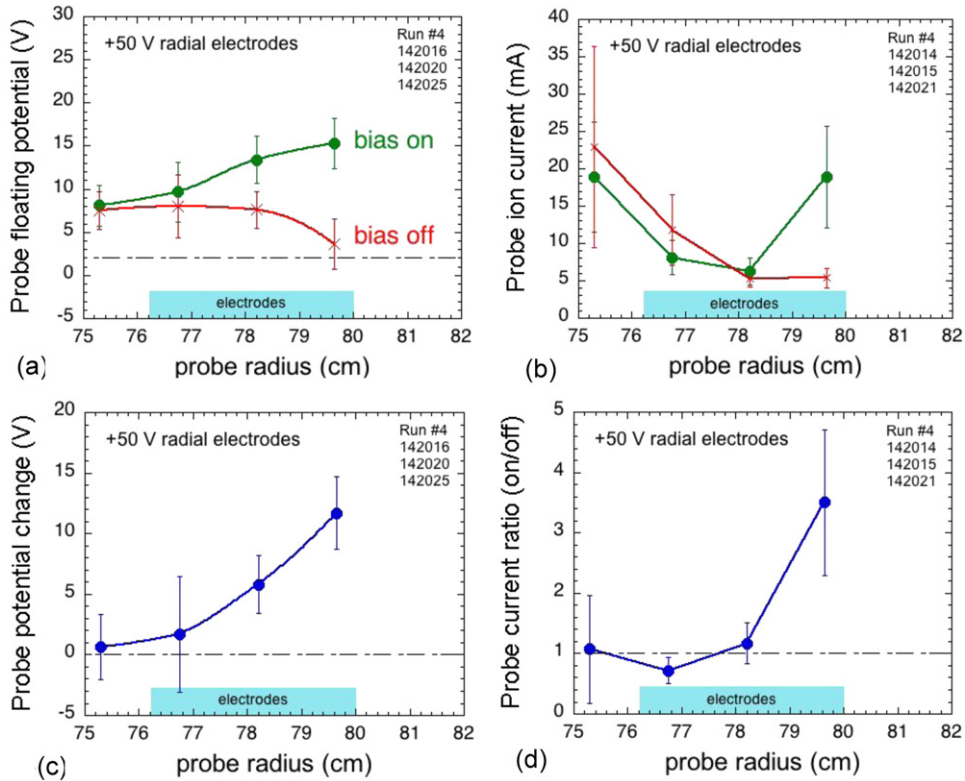


Figure 5. Probe responses to radial electrode biasing averaged over many bias ‘bias on’ and ‘bias off’ cycles for run #4. When the electrodes are biased, these probes show an increase in floating potential at the large major radius end of the electrodes as shown in (a), and an increase in probe ion saturation current at the largest major radius probe as shown in (b). The potentials change by about +10–15 V at the top probe and the probe currents increased by a factor of 3–4 at the largest major radius probe, as shown in (c) and (d). The ratios in (d) are the averages of the individual on/off ratios in each cycle, not the ratio of the average on/off levels of (b).

plotted as a function of radius (with standard deviations shown by the error bars). The floating potential differences between ‘bias on’ and ‘bias off’, as shown in figure 5(c), were +10–15 V at largest major radius probe R2, about +5 V at probe R3, but nearly zero at probes R4 and R5. Figure 5(b) shows the probe ‘bias on’ and probe ‘bias off’ ion currents (at -50 V probe bias) evaluated in a similar way. These probe currents increased by a factor of over $\times 3$ at the outermost probe R2, with no significant increases at R3, but with a fairly clear *decrease* in probe current at R4, as illustrated in figure 5(d). A similar effect was seen when the probes were biased at +50 V to collect electrons, showing that these effects were due to changes in the local density and not due to changes in local potential.

3.1.2. Effects in the images from the camera. We now discuss the camera data for this run. Camera views of the electrode region during this run were only available in Li I light, which can be qualitatively interpreted as showing where and when the local plasma is affected by biasing (see section 2.3). Some examples of these images are illustrated in figure 6, where each image shows a $\sim 15 \text{ cm} \times 15 \text{ cm}$ region around the radial electrodes. The exposure times were $1 \mu\text{s}$ and the spatial resolution was $\sim 0.8 \text{ cm/pixel}$ in this view. The approximate electrode locations are shown by the rectangular boxes and the probes are located along the line to the left of the electrodes. The radially outward direction is upward and the magnetic field

direction is to the right, as shown by the arrows at the lower left in each panel.

The images in figure 6 are taken with either ‘bias on’ (left) or ‘bias off’ (right) for three shots in this run. The top and middle rows were for the first biasing cycles of these shots (#142016 and #142014), while the bottom row was taken during a later biasing cycle in a similar shot (#142020). The brightest feature in all these images is a toroidal arc running horizontally across the images, which indicates the location of the highest particle/heat flux zone region near the OSP. This strike zone passes through the electrodes in the top row, and is $\sim 3 \text{ cm}$ inboard of the lower edge of the electrodes in the bottom two rows (the magnetic OSP locations are $\sim 1\text{--}3 \text{ cm}$ farther outward than these visible strike zones). A comparison of the ‘bias on’ images at the left with the ‘bias off’ images at the right shows that the biasing did not affect the location of this bright arc (or the magnetically derived OSP), except for a localized increase at the upper half of the electrodes at the top left of figure 6. During later biasing cycles the electrodes themselves began to glow brightly, as shown in the two images at the bottom of figure 6. This electrode glow is seen during both ‘bias on’ and ‘bias off’ periods, as discussed below.

These local effects of the biasing near the electrodes are more clearly isolated by normalizing the images with ‘bias on’ to those with ‘bias off’. Four such image ratios are shown in figure 7 for the same camera view and shot used for the middle row of figure 6. The false-color intensity scale now goes from

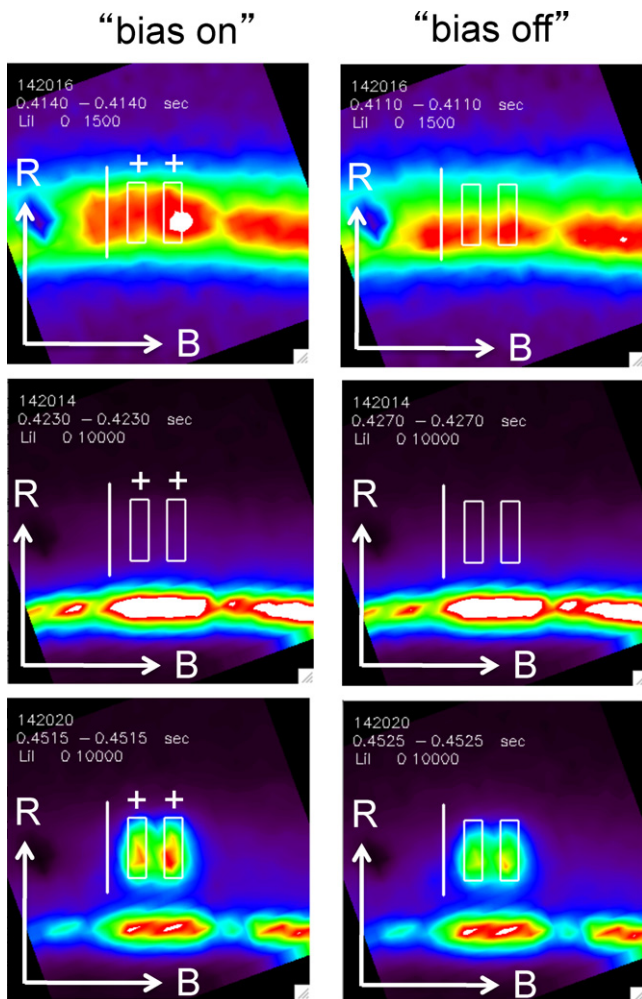


Figure 6. Camera images of Li I light in the region of the radial electrodes taken with a $1 \mu\text{s}$ exposure time during shots with electrode biasing. The colors show the light level from zero (black) to maximum (red/white). The electrode regions are shown by the white rectangles, the probes are along the line to the left of the electrodes, and the radially outward direction is upward. The bright horizontal arcs are where the largest heat/particle flux hits the divertor plate and the tile holding the electrodes. The images at the left were taken during ‘bias on’ periods, and the images at the right were taken during ‘bias off’ periods.

0.5 (black) to 2.0 (red/white). At the top left of figure 7 is the ‘bias on’ to ‘bias off’ ratio for 1 ms periods just after and before the rise time of biasing. The image at the top right is the ‘bias on’ over ‘bias off’ ratio for 1 ms periods just before and after the fall time of biasing. In both cases the Li I light level increases by a factor of ~ 2 at the large major radius end of the electrode during biasing, and this increased Li I signal extends ~ 4 cm toroidally to the nearby probes. Similar images are shown at the bottom of figure 7 for longer averaging intervals of 6 ms for the first biasing cycle (left) and the fourth biasing cycle (right), showing that the prompt increase in light at the top of the electrodes persists during biasing, and also during the electrode glow later in the shot. Similar changes in the Li I light emission pattern were observed in all other run.

Thus the Li I light level increased at the large major radius end of the electrodes near the same major radii where the probe

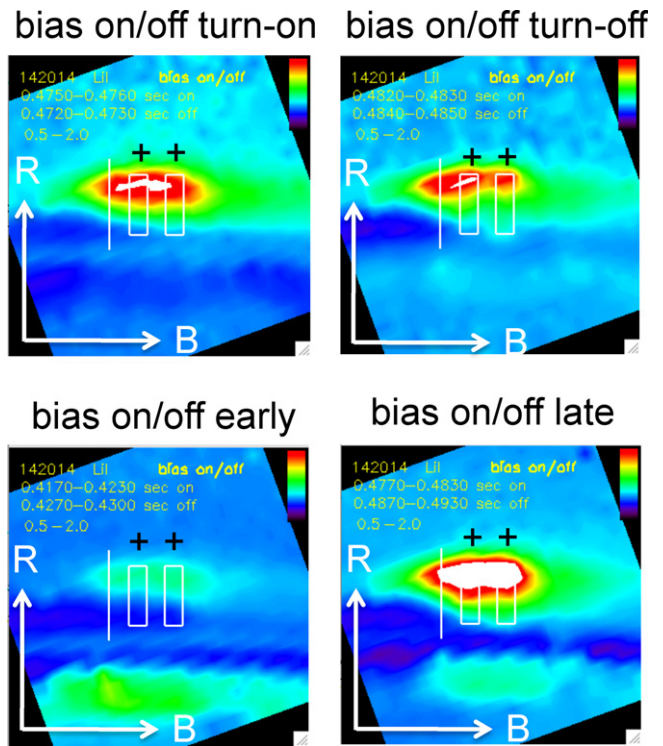


Figure 7. Images showing the ratio of the Li I light emission for ‘bias on’ to ‘bias off’, with the same field of view as for figure 6. The top figures show this ratio for 1 ms time intervals around the rising (left) and falling (right) periods of the biasing. The color scale for this ratio ranges from black (0.5) to red/white (2.0), as shown at the upper right in each image. At the bottom are similar ‘on/off’ ratios but averaged over 6 ms periods during ‘bias on’ and ‘bias off’ cycles for the same shot.

potential and probe current increased in figure 5. There was also a trend for the Li I light ratio to decrease at the small major radius end of the electrodes where the probe current decreased slightly in figure 5, but this was less clear.

Further information on the time dependence of the Li I light from the electrode region for this shot is shown in figure 8, along with the electrode voltage signals. The two separate curves in the upper part of figure 8 are the average Li I light levels within the larger major radius half (i.e. ‘top’) of the electrode area (including the space between the electrodes), and for the smaller major radius half (i.e. ‘bottom’) of the electrode area (including the space in between the electrodes). The light from the top half of the electrode showed a large prompt (< 1 ms) rise with biasing, whereas the light from the bottom half of the electrode showed little or no immediate rise. The Li I light also increased slowly over ~ 50 ms due to the electrode glow effect in both the top and bottom half of the electrodes, as shown at the bottom of figure 6.

The lower part of figure 8 shows the time dependence of the ratio of the top to bottom electrode light levels for this same shot. The times used for the rising and falling ‘bias on’/‘bias off’ frame ratios in figure 7 are also indicated by the arrows. This top/bottom ratio increases within < 1 ms by $\sim 30\%$ with every ‘bias on’ cycle, at least for the first ~ 100 ms. This same type of difference between ‘bias on’ and ‘bias off’ was also seen in 6 ms long time averages taken during the middle of both early

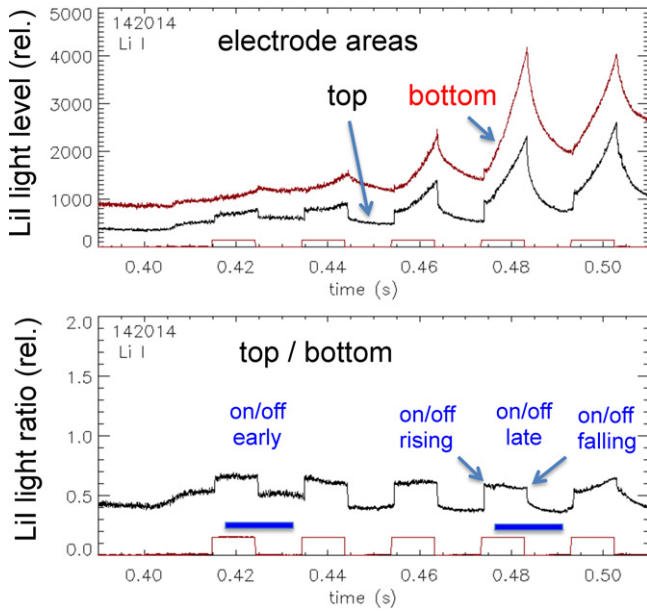


Figure 8. Time dependence of the Li I light emission at the top and bottom of the electrodes for the shot of figure 7. The light in the top region has a relatively large prompt increase with every bias cycle, and a slower increase corresponding to the electrode glow shown at the bottom of figure 6. The light from the bottom of the electrode has little or no prompt increase with biasing, but does show a slow increase corresponding to the electrode glow. The ratio of the top/bottom signals is shown in the lower part of the figure, along with the times used for the image ratios in figure 7.

and late bias periods in this shot, as shown by the two images at the bottom of figure 7 for the times indicated in the lower part of figure 8. The prompt top/bottom asymmetric effect of biasing was seen in most bias cycles in this run, but the time-averaged top/bottom asymmetry was sometimes obscured by the slow time evolution of the electrode glow at later times during the biasing. The electrode heating and glow are discussed further in section 4.5.

In summary, a positive biasing of the two radial electrodes caused a prompt (<1 ms) increase in the probe floating potential and probe current signals near the larger major radius end of the electrodes, but had relatively little effect on the probes at the small major radius end of the electrodes (figures 4 and 5). The Li I light levels seen by the camera also showed a prompt increase at the large major radius end of the electrodes with biasing (figures 7 and 8). These results are both qualitatively consistent with an increase in density at the large major radius end of the electrodes. However, the OSP as seen in the Li I light was *not* displaced during biasing (figure 6), and no other effect of this electrode biasing was seen in any other region of the plasma.

3.2. Toroidal electrodes far outside the OSP

This section describes cases in which a small local effect due to electrode biasing could be seen only using a magnified camera view of the electrodes. These were H-mode plasmas from run #2 (see table 1), with plasma parameters similar to those for run #4 of section 3.1. In these cases the outer (larger major radius) toroidal electrode was biased at +90 V but drew a relatively

small current of ~ 10 A, and the inner toroidal electrode was biased at -90 V and drew ~ 1 A. The outer divertor strike point for this run was ~ 10 – 14 cm radially inside the toroidal electrodes, i.e. much farther away from the electrodes than for the cases of section 3.1.

3.2.1. Effects in the nearby Langmuir probes. Figure 9 shows typical electrode voltages and currents for this run at the top, along with typical probe floating potential and probe electron currents for this run. The nearby probe signals T1, T3 and T5 show no visible effects of the electrode biasing on either the floating potentials in figure 9(a) or the probe currents in figure 9(b), which were taken at a probe bias of +50 V (due to the small plasma density near the probes for this run). The other two probes signals from T2 and T4 (not shown) look similar. This contrasts sharply with the cases previously shown in figure 4 in which there were clear effects of biasing on some of the probes. Another difference between the probe signals in figures 9 and 4 is that the fluctuations completely dominate the probe signals in figure 9 (with or without biasing), but are relatively small in figure 4. This is apparently due to the larger relative fluctuation level in the far-SOL (figure 9) compared with the near-SOL (figure 4).

Figure 10 shows the effects of electrode biasing in run #2 on the radial profiles of the probe floating potentials and probe electron currents. The floating potential *differences* between the ‘bias on’ and the next ‘bias off’ cycle are shown in figure 10(a), and the probe current *ratios* for ‘bias on’ to the next ‘bias off’ are shown in figure 10(b). These are averaged over many bias on-off cycles with the standard deviations shown as error bars. There were no consistent changes associated with biasing, although there may be a slight effect in the outermost probe, which was just above the top of the positively biased electrode. This contrasts with the results of section 3.1 in which there were clear changes in probe signals with biasing (figure 5).

3.2.2. Effects in the images from the camera. We turn now to the camera data for run #2, which had a more highly magnified view of the electrodes than for run #4. In the top row of figure 11 are five images of the toroidal electrodes with ‘bias on’, and in the bottom row are images in the next ‘bias off’ cycle. All images are single frames with a relative intensity range shown in the figure labels, e.g. 300–700 counts is the black-to-white range in figure 11(a). In figure 11 the center of the positive electrode is marked by the ‘+’. The probes were at the lower left of the electrodes but too small to see in these images.

In the left column of figure 11 are images taken with a D_α filter at an exposure time of $8 \mu\text{s}$. These images show the two toroidal electrodes within a region $\sim 15 \text{ cm} \times 15 \text{ cm}$ similar to that of figure 1, but rotated counter-clockwise $\sim 50^\circ$. The ~ 1 – 2 mm wide gap between the electrodes and the surrounding tile can be resolved with this magnified view. In these D_α light image there is no difference between the ‘bias on’ image in (a) and the ‘bias off’ image in (b) in this (or any other) bias cycle in this run. There are also no signs of turbulent fluctuations in these images. This suggests that the observed light is due to

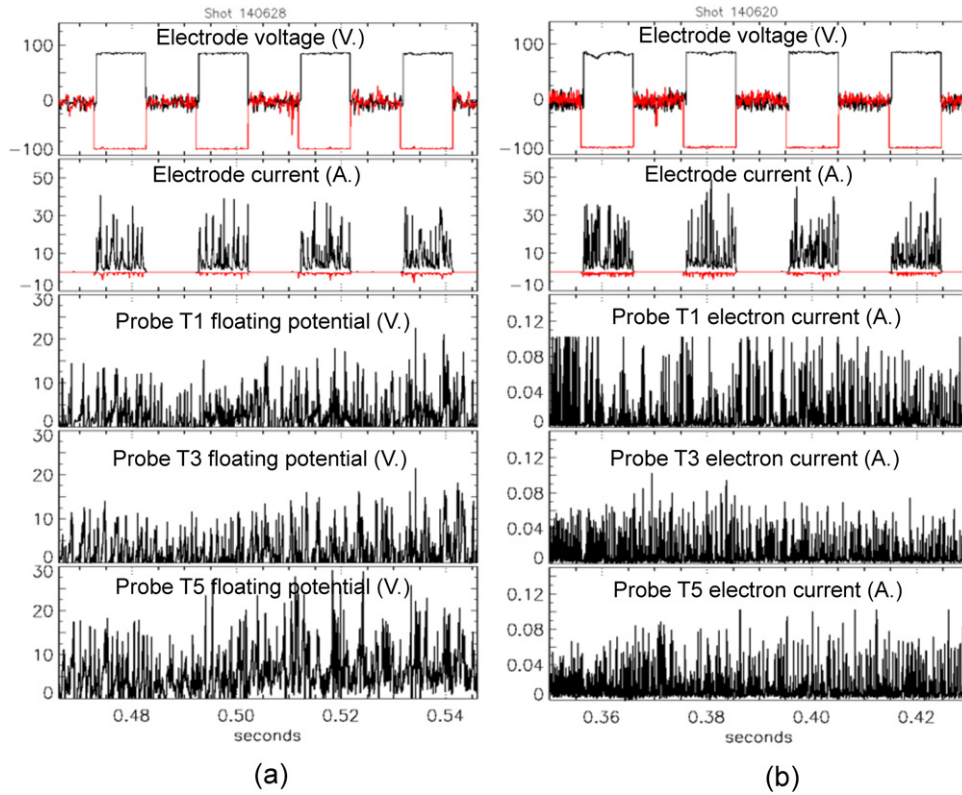


Figure 9. Electrode and probe signals versus time for typical shots during biasing of the toroidal electrodes (run #2). The electrode voltages and currents are shown at the top. The upper electrode is positively biased at +90 V in these shots and draws ~ 10 A, while the bottom electrode is biased at -90 V and draws ~ 1 A. Three probe floating potential signals are shown at the left, and three probe electron currents are shown at the right (for a +50 V probe bias). These probes correspond to the locations shown at the left of figure 2. There were no clear effects of the electrode biasing on these probes, or on probes T2 and T4 (not shown).

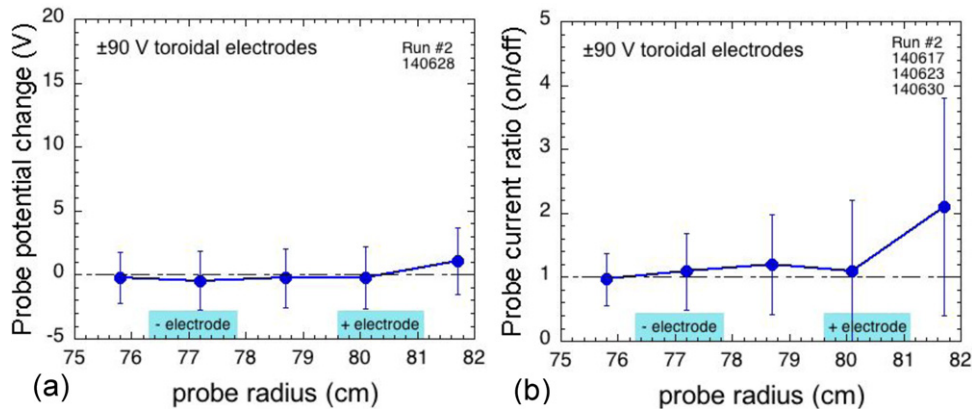


Figure 10. Probe responses to toroidal electrode biasing averaged over many ‘bias on’ and ‘bias off’ cycles for run #2, in which the OSP is relatively far from the electrodes. There were no clear changes in the probes in response to this type of biasing, outside the standard deviation.

reflections from elsewhere, and that the recycling light from D_α is not significant at this location (probably due to the lithium coating during these runs).

The three pairs of images 11(c)–(h) were taken with the same field of view as 11(a) and (b) but with a Li I filter with a 3 or 4 μs exposure time. The bright lines running diagonally across these images are single turbulence filaments or ‘blobs’, as described previously [23]. The location of these intermittent filaments vary on a $\sim 10 \mu\text{s}$ frame-to-frame timescale, but they are very nearly toroidally aligned at the divertor plate

(with or without biasing). These filaments cause the strong fluctuations seen in the probe signals of figure 9. The frames used in figures 11(c)–(h) were chosen to have these filaments intersecting the center of the positively biased electrode shown by the ‘+’ mark.

For the image in figure 11(c) there is a ~ 0.5 cm outward deflection of the filament near the ‘+’ mark, and for figures 11(e) and (g) there is a dark region covering the bottom (smaller major radius) half of the outer electrode. No similar deflections or dark regions were observed near the

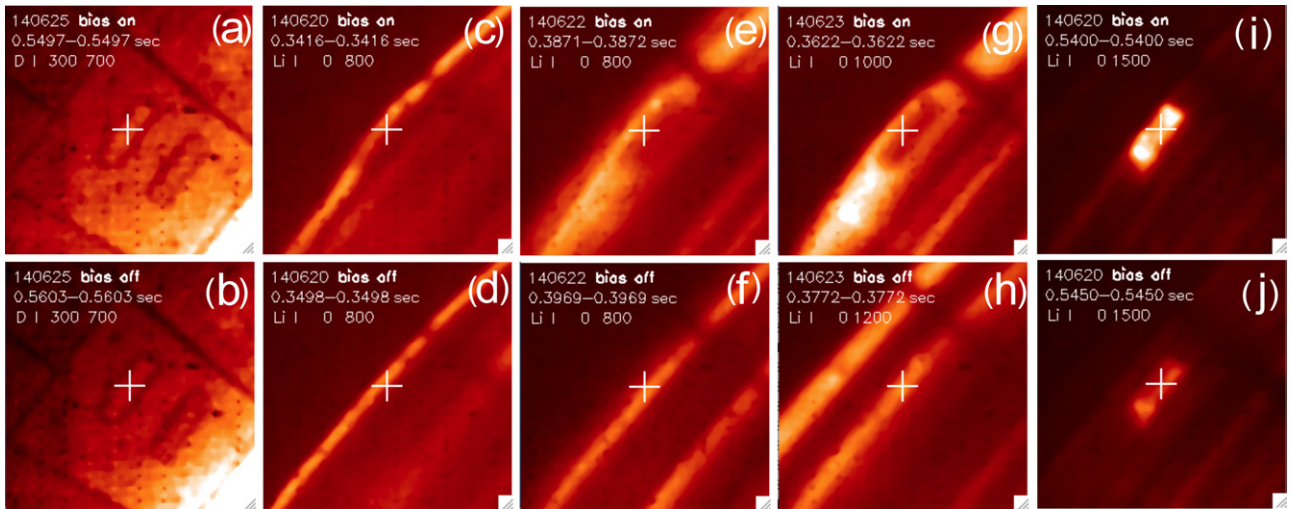


Figure 11. Images of the toroidal electrodes for run #2 taken with a ~ 1 – 2 mm spatial resolution. In the top row are images during ‘bias on’, and in the bottom row are images taken during the following ‘bias off’ cycle. At the left is a view in D_α light which shows the electrode locations, in the middle are three pairs of images taken in $Li I$ light, and at the right are images taken with an IR filter. The middle images show an intermittent dark region which appear during biasing within the lower (small major radius) half of the positive electrode. The right images show the electrode glow effect in $Li I$ light.

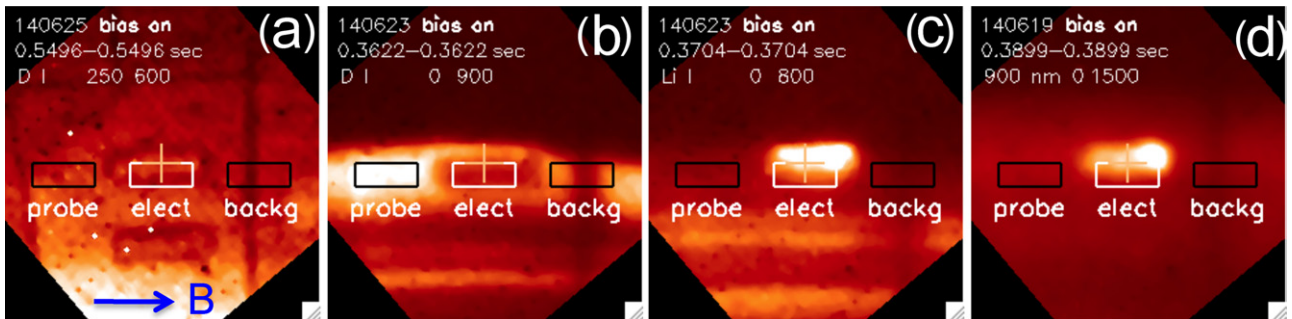


Figure 12. Images similar to those of figure 11 but with boxes drawn to show the location of the regions used to evaluate the time-dependent changes in the electrode light emission in figure 13. The ‘electrode box’ covers the lower half of the upper toroidal electrode. The ‘probe box’ and ‘background box’ are located at the same major radius in order to minimize the effects of turbulent fluctuations in the analysis.

negatively biased lower electrode, or in any frames without biasing, for example, in figures 11(d), (f) or (h). The frames in figures 11(c)–(h) were taken during one of the first few biasing cycles in these shots, but not all frames during this time had similar deflections or dark regions.

The frames in figures 11(i) and (j) were taken about 200 ms later in the same shot as figures 11(c) and (d), but show a bright emission at the positive electrode during both the ‘bias on’ period and (to a lesser extent) during the ‘bias off’ period. A similar electrode glow was seen in all other shots and also in the radial electrodes (e.g. figure 6). This glow is most likely due to electrode surface heating, as discussed in section 4.5.

Figure 12 shows four images similar to those in figure 11, but now rotated so that the toroidal direction is horizontal, with the center of the outer positive electrode again marked by a ‘+’. Figure 12(a) was taken with a D_α filter, and shows the location of the electrodes for orientation. Figure 12(b) was taken with a $Li I$ filter and shows the dark region at the bottom of electrode. Figure 12(c) was taken with a $Li I$ filter 40 ms later in the same shot as for figure 12(b), and shows an example of the electrode glow, which is not located in the same place as

the dark region. Figure 12(d) was taken with a filter in the IR band 900–1100 nm and also shows the electrode glow.

Each frame in figure 12 also has three boxes used for the analysis below. The white ‘electrode’ box in the middle of each frame is drawn to overlap the dark region at the bottom of the electrode in figure 12(b). This box has a size 2.9 cm toroidal \times 1.1 cm radial and is located just below the ‘+’ mark. Each frame also has two black boxes of the same size and radial location as the white box, but centered ± 4.6 cm toroidally from the center of the white box. The black ‘probe’ box at the left is in the region near probe T2, which is upstream along the B –field line intersecting the electrode, while the black ‘background’ box on the right is downstream along B , and used as a background reference region at the same major radius. Note that the camera view holds steady to within ~ 0.1 cm over this time.

The top panel in figure 13 shows the time dependence of the average $Li I$ light level within the ‘electrode box’ for a 120 ms period of the shot used in figures 12(b) and (c). The electrode voltage traces are also shown at the bottom of the figure. The $Li I$ light level has large fluctuations with or without biasing, and it is difficult to see any systematic

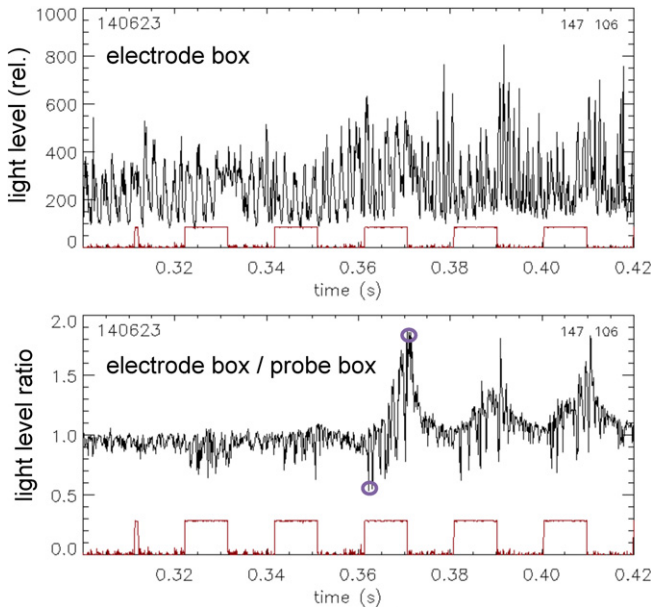


Figure 13. The top panel shows the large time-dependent fluctuations of the Li I light from the ‘electrode box’ of figure 12. The bottom panel shows the ratio of the signals from the ‘electrode box’ divided by the ‘probe box’ of figure 12. This ratio shows a time-dependent intermittent $\leq 30\%$ decrease corresponding to the dark regions in the lower half of the electrode shown in figures 11 and 12. The slowly growing electrode glow is also apparent at later times. The circled points at the bottom show the times for the middle frames of figure 12.

changes with biasing, as was also the case in the probe signals of figures 9 and 10. These fluctuations are due to the turbulence filaments which randomly cross this analysis box on a timescale of $\sim 10 \mu\text{s}$ and (in this case) to a coherent low-frequency oscillation at $\sim 0.5 \text{ kHz}$.

The bottom panel in figure 13 shows the ratio of the signal in the ‘electrode box’ to that in the ‘probe box’ as a function of time for the same shot. This ratio is much less sensitive to turbulent fluctuations since these two boxes are at the same major radius and therefore see nearly the same turbulence filaments. There are systematic but intermittent $\sim 10\text{--}30\%$ decreases (i.e. sharp downward spikes) in this ratio during all biasing periods, along with a slower increase in this ratio during the later cycles due to the electrode glow effect. The times used for figures 12(b) and (c) are shown by circles in the bottom. The ratio of the ‘electrode box/background box’ is similar to the ‘electrode box/probe box’ of figure 13, suggesting that the main effect is a darkening within the electrode box.

All other shots in this run show similar intermittent decreases in this ‘electrode box/probe box’ ratio during biasing during the first 50 ms of biasing; however, the time-averaged of this ratio decreased by only $\sim 10\%$ with biasing. All shots also showed slow increases in this Li I light ratio for later cycles due to the electrode glow effect, with similar behavior seen using an IR filter (at $400 \mu\text{s}$ exposure time). This same ratio with a D_α filter show neither the intermittent decreases nor the increases due to electrode glow, again indicating that the D_α was from reflected light.

In summary, positive biasing of one toroidal electrode far outside the OSP in run #2 caused little or no systematic

effects in the nearby probes (figures 9 and 10). However, the bottom half of this electrode showed intermittent time-dependent decreases during biasing, as shown in figures 11–13. The light emission near the negatively biased electrode did not change with biasing in any light emission band, and no other effects of this electrode biasing were seen in any other region of the plasma.

3.3. Effects of electrode biasing in other runs

Figure 14 shows the probe results from the only other run with a significant effect of electrode biasing (run #5). For this run both toroidal electrodes were biased positively and the OSP was just inside the major radius of the inner toroidal probe. The average total electrode current in this run was $\sim 38 \text{ A}$, i.e. nearly as high as for run #4 (see table 1). Changes in the probes were only seen near the inner toroidal electrode (T4), where floating potential increased by about $+5\text{--}10 \text{ V}$ and the ion saturation current increased by a factor of ~ 1.5 . Unfortunately, the camera could not see clear changes near the electrodes for this run since the turbulence level was almost as high as for run #2, but the camera magnification was relatively low as for run #4, so small-scale changes in light emission could not be resolved.

The other two runs (#1 and #3) were performed with one radial electrode biased positively or both toroidal electrodes biased positively. In these cases the OSP was usually far inside the electrodes, and the average total electrode current were only $\sim 1 \text{ A}$ and $\sim 2.3 \text{ A}$, respectively (see table 1). No significant changes were visible in either the probes or in camera data for electrode biasing in either of these runs.

Figure 15 shows the probe floating potential changes and probe current ratios versus the total positive current for all five runs in this experiment. Each point represents one on-off bias cycle in one shot. The data points from runs #1 and #3 all had $\leq 10 \text{ A}$ and showed no trend with total current. The data points from run #2 were in the total current range $\sim 4\text{--}20 \text{ A}$ but also showed no trends with electrode current. Thus the increases with electrode current in figure 15 were from runs #4 and #5, in which both electrodes were positively biased and the OSP was relatively near the electrodes.

In summary, when two the toroidal electrodes were biased positively, the probe near the electrode closest to the OSP showed increases in potential and current similar to those seen in section 3.1. In the overall probe database, these probe effects increased with total electrode current over the range of $\sim 20\text{--}80 \text{ A}$, but no significant effects were observed for $\leq 20 \text{ A}$. These probe changes were similar for both the radial and toroidal electrode geometries.

3.4. Absence of non-local effects of the electrodes

No effects of this divertor electrode biasing were seen on any global plasma parameters or on any diagnostics more than a few centimeters away from these electrodes. This is not too surprising, since these electrodes occupied only $\sim 1\%$ of the toroidal circumference of the tokamak at the OSP.

For example, the location of the highest particle/heat flux near the OSP was monitored by the position of toroidal band

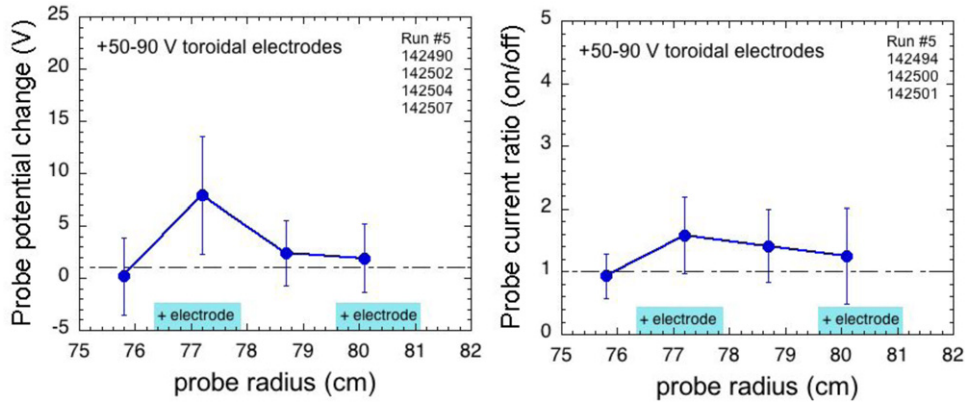


Figure 14. Probe responses to toroidal electrode biasing averaged over many ‘bias on’ and ‘bias off’ cycles for run #5, in which both electrodes were biased positively and the OSP is just inside the electrode major radius. There are marginally significant increases in the probes signals near the innermost positive electrode at $R \sim 77.5$ cm in these cases.

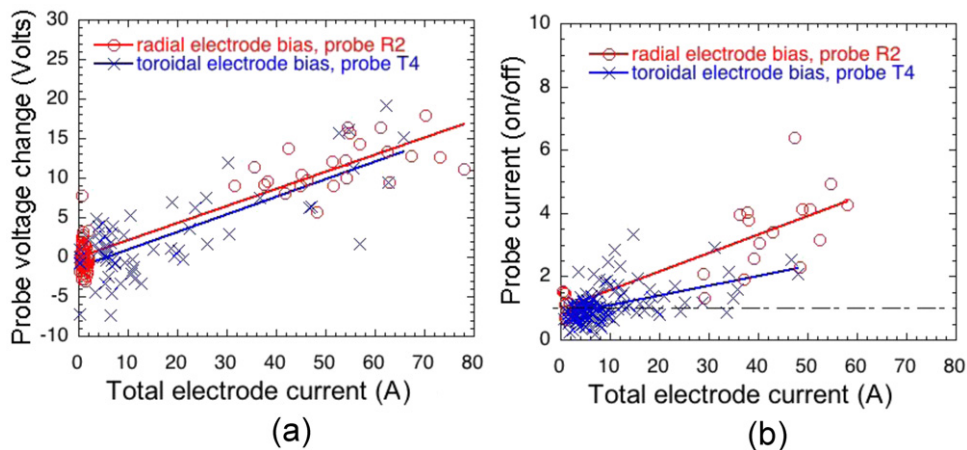


Figure 15. Responses of the probes R2 and T4 to electrode biasing in the entire database of table 1. Each point corresponds to one bias on-off cycle. At the left is the variation in these probe floating potentials with the total positive biasing current, and at the right is the variation in the ratio of these probe currents with/without biasing. The probe potentials and currents increase with electrode current for ≥ 20 A, corresponding to data from runs #4 and #5 in which the electrodes were near the OSP.

of Li I light for run #4 (as illustrated in figure 6). The radial location of the OSP measured this way (or with magnetic diagnostics) did not change with biasing, even in the shots with the largest local effects. No magnetic perturbations due to electrode currents were seen on the MHD fluctuation diagnostic arrays (although the system noise was comparable to the expected B -dot signals at this low frequency). No evidence for effects of biasing on ELMs were seen in these experiments; in fact, large spikes due to the ELMs were clearly seen in the electrode and probe currents during ‘bias on’ periods in H-mode. No evidence for an influx of impurities due to electrode biasing was seen in the radiated power or edge x-ray emission.

4. Discussion

The goal of this paper was to characterize the effects of small non-axisymmetric divertor plate electrodes on the local SOL plasma in NSTX. An overview of the experimental results is given in section 4.1, a qualitative description of the expected convective cell pattern is given in section 4.2, and the calculated

structure of the magnetic flux tube attached to such an electrode is described in section 4.3. A preliminary attempt at quantitative modeling is discussed in section 4.4, the electrode heating and glow effects are discussed in section 4.5, and conclusions and directions for further research are presented in section 4.6.

4.1. Overview of experimental results

Four small electrodes were installed into the outer divertor plates of NSTX, as shown in the photos of figure 2. Several runs were made in which each electrode was biased positively from +50–90 V, as listed in table 1. The local effects of this biasing were measured using the Langmuir probe and camera diagnostics discussed in section 2. The main results as described in section 3 can be summarized as follows:

Section 3.1. When both radial electrodes were biased at +50 V near the OSP, there was an increase in the probe currents and potentials (figures 4 and 5) and the Li I light emission (figures 6–8) near the top (large major radius end) of these

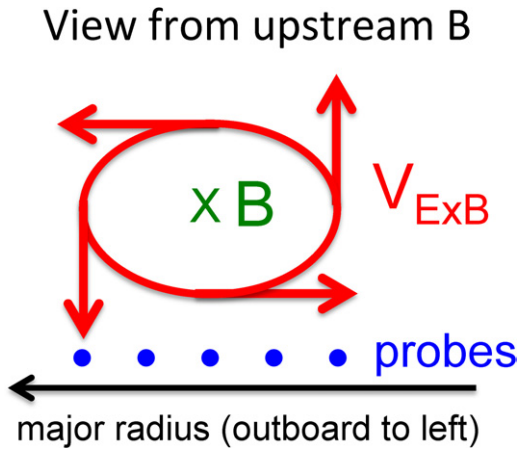


Figure 16. Schematic illustration of the convective cell of figure 1 as viewed from upstream along B toward a positively biased circular electrode on the divertor plate. The expected $E \times B$ convective motion is downward into the surface probes at larger major radii, radially inward along the divertor surface at the middle of the cell, and upward from probes at the inner major radii.

electrodes. These effects were localized to within a few cm of the electrodes and occurred on a fast timescale of <1 ms.

Section 3.2. When one toroidal electrode was biased at $+90$ V farther out from the OSP, there were no clear effects on the nearby probes (figures 9 and 10), but there was an intermittent time-dependent decrease in the Li I light emission within the bottom half of this electrode (figures 11–13).

Section 3.3. When both toroidal probes were biased at $+50$ – 90 V near the OSP, there was an increase in the probe currents and probe potentials only near the inner electrode (figure 14). In the entire probe database, the effects of biasing increased with the total electrode current up to ~ 80 A, but were negligible below ~ 20 A (figure 15).

Section 3.4. There were no observable non-local effects of this electrode biasing in any other diagnostic in these plasmas.

4.2. Qualitative picture of expected convective cells

A simple schematic picture of the expected convective cell pattern around a biased circular electrode at a divertor plate was shown in figure 1. This picture assumed that the B -field line intersected the electrode at a small angle, and that the convective cell extended along B . Figure 16 shows another perspective of this convective cell pattern, now looking from the direction along B toward the circular electrode. The magnetic flux tube is a flattened cylinder with vertical height to radial width ratio of ~ 0.25 since the angle between the B -field line and the divertor plate is $\delta \sim 15^\circ$ (e.g. for run #4). Since the B -field is pointing into a positively biased electrode, the $E \times B$ flow should be counter-clockwise in this view.

Therefore the local $E \times B$ flow should have a dominantly inward horizontal component at the radial probe located below the center of the convective cell, which should cause an inward

plasma displacement as suggested in figure 1. Since the average plasma density and heat flux are decreasing functions of major radius outside the OSP, it is not at first apparent how this displacement could cause the increase in density at the large major radii end of the electrodes as seen in these experiments.

However, there should also be a vertically downward $E \times B$ component toward these surface probes at the outer (large major radius) edge of the convective cell, and a vertically upward component at the inner (small major radius) edge of the convective cell. These vertical flows might help us to qualitatively explain the two main effects seen with biasing in this experiment: the increased probe current and light emission seen at the larger major radii in figures 5 and 7, and the decreased light emission seen in the lower half of the electrodes in figures 11–13. In the first case, the downward $E \times B$ flow would push plasma into the probes, and in the second case, the upward $E \times B$ flow would prevent plasma from hitting the inner half of the electrode.

This discussion suggests that even a qualitative interpretation of the results of experiment requires some knowledge of the 3D spatial structure of the local electric fields and plasma parameters. A preliminary approach to such modeling is discussed in the next two sections.

4.3. Electrode flux tube shape

It will eventually be important to know the structure of the magnetic flux tubes attached to the electrodes in this experiment. These shapes could in theory affect the flow of plasma to the electrode region; for example, the convective cell might terminate where the width of the flux tube becomes narrower than an ion gyroradius [2, 3]. The left side of figure 17 shows magnetic flux surface plots for one shot in this experiment (from run #4), along with the projected path of a field line connected to an electrode about 4 cm outside the OSP in this shot (i.e. starting at $R = 80$ cm). The ‘+’ marks on this field line are made every 1 m along B ; thus the X-point height is reached after ~ 2 m, and the outer midplane is reached after ~ 7 m.

Due to the $\sim 15^\circ$ angle of the B -field line with respect to the divertor surface, the cross- B -field width of the toroidal electrodes is ~ 1 cm immediately just above the electrodes, and $\sim 1/4$ cm for the radial electrodes. As these flux tubes move along B toward the X-point, their shapes become ‘squeezed’ by magnetic shear into a ribbon-like structure [25], so that 2 m from the electrodes they become very thin, as shown in figure 17(b). The resulting cross-field widths in the plane perpendicular to B versus the distance along B from the electrodes are shown in figure 17(c). Since a typical ion gyroradius at $T_i \sim T_e \sim 15$ eV (see below) and $B = 0.5$ T is ~ 0.1 cm, these flux tubes are an ion gyroradius wide at $\sim 2 \pm 1$ m along B . Thus if the parallel extent of the convective cell is limited by the ion gyroradius, the cell should not extend much above the X-point in this configuration.

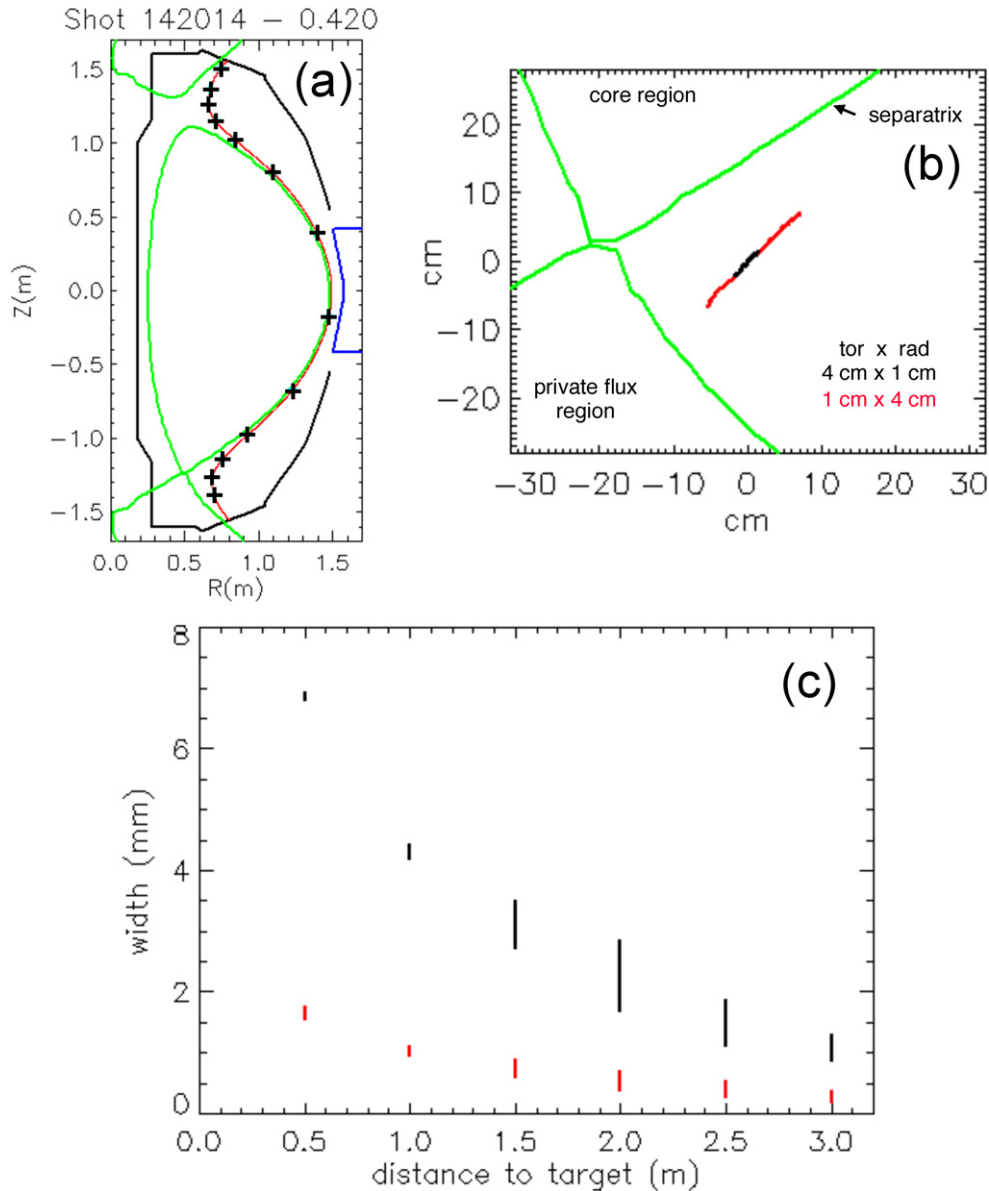


Figure 17. In (a) is a plot of the NSTX flux surfaces for the shot of figure 7, along with the path of a field line hitting the divertor plate at $R = 80$ cm. There is a '+' mark every 1 m along B . In (b) is a close-up view near the lower X-point showing the cross- B -field shapes of the flux tubes for both electrodes. In (c) is the cross- B -field width of these flux tubes for both electrodes as a function of the distance along B to the divertor target plate. The vertical ranges in these widths are due to variations across the electrode cross-section.

4.4. Preliminary attempt at quantitative modeling

A quantitative model for this biasing experiment would need to evaluate the 3D electrostatic potentials near the electrodes to find the cross-field flows associated with the biasing. This modeling should be similar to that for the difficult and longstanding issue of ion and electron collection in flush-mounted Langmuir probes [26–30]. In both cases the main problem is to understand the cross-field mobility and current paths in the plasma near the electrode or probe flux tube. This model will depend on many factors such as the flux tube geometry, the local plasma parameters, the ion orbit size, the local turbulence, the local plasma flows and the ion-neutral collision rate, each of which can influence the potentials across and along B and so determine the 3D structure of the convective cell. Once these convective cell patterns are

known they could be used to modify any existing model for the local heat and particle flows without biasing. Given the many uncertainties in this process, only a preliminary approach is described here.

Rough values for some plasma parameters near the electrodes are given in table 2 for the case in which the electrodes were near OSP (section 3.1). Plasma densities of $n \sim (5\text{--}10) \times 10^{12} \text{ cm}^{-3}$ (with an uncertainty of at least a factor of 3) were estimated from the probe ion saturation current of $\sim 5\text{--}10$ mA (see figure 5) and the projected probe tip surface area perpendicular to B of $\sim 5 \times 10^{-3} \text{ cm}^2$. An electron temperature of $T_e \sim 10\text{--}20$ eV (with an uncertainty of at least a factor of 2) was obtained from fitting voltage sweeps of probes R2–R5 between the ~ 0 and $+40$ V. These densities and temperatures are roughly similar to those measured independently by another probe array ~ 3 cm outside the

Table 2. Parameters for preliminary modeling.

Electron density:	$n \sim (5-10) \times 10^{12} \text{ cm}^{-3}$
Electron temperature:	$T_e \sim 10-20 \text{ eV}$
Neutral density:	$\sim 10^{10}-10^{11} \text{ cm}^{-3}$
Debye length:	$\sim 10^{-3} \text{ cm}$
Ion gyroradius (assuming $T_i = T_e$):	$\sim 0.1 \text{ cm}$
Perpendicular scale length of cells:	$\sim 1 \text{ cm}$
Parallel scale length of cells:	$\sim 2 \text{ m}$
Potential inside convective cells:	$\leq 50 \text{ V}$
Estimated $v_{E \times B}$ velocity of cell:	$\sim 2 \times 10^5 \text{ cm s}^{-1}$
Poloidal turbulence velocity:	$\sim 10^5 \text{ cm s}^{-1}$
Local poloidal flow velocity:	$\sim 10^5 \text{ cm s}^{-1}$

OSP [24]. The neutral deuterium density of $n_0 \sim 10^{10}-10^{11} \text{ cm}^{-3}$ was estimated (order-of-magnitude) by assuming an incident deuterium ion flux of $\sim 10^{-2} \text{ A cm}^{-2}$ with a recycling coefficient of 1 and a neutral deuterium speed corresponding to $\sim 2 \text{ eV}$.

A very important but unmeasured parameter in this problem is the profile of the potential within the electrode flux tube with biasing. The measured floating potential changes were at most $\sim 10-15 \text{ V}$ for a $+50 \text{ V}$ bias (figure 4), but this was at a probe located $\sim 0.3-0.4 \text{ cm}$ across B from the flux tube defined by the nearest radial electrode. If the potential inside this flux tube did not produce a local maximum in the electrostatic field, then no convective cell should form. Although it might be possible to model the 3D electric fields around the electrodes given the parameters of table 2, such modeling is beyond the scope of this paper.

Instead, following the discussion of [19], we will make some assumptions in order to estimate the number of rotations N of the plasma in this convective cell over its length along B as: $N = v_{E \times B}(L_{\parallel}/v_{\parallel})/(2\pi L_{\perp})$, where $v_{E \times B}$ is the cell velocity, L_{\parallel} is the parallel length of the cell, v_{\parallel} is the parallel ion flow speed and L_{\perp} is the cross-field scale length of the cell. Assuming $L_{\perp} \sim 1 \text{ cm}$, then $E_{\perp} \sim 10 \text{ V cm}^{-1}$ and $v_{E \times B} \sim 2 \times 10^5 \text{ cm s}^{-1}$. Thus if $L_{\parallel} \sim 2 \text{ m}$, and $v_{\parallel} \sim 2 \times 10^6 \text{ cm s}^{-1}$, we find $N \sim 3$. This implies that a convective cell could move the plasma significantly within an ion transit time along the cell length, which makes it plausible that the cell produced by these electrodes could cause local changes in the plasma near the electrodes.

Other complicating factors will eventually have to be considered in quantitative modeling. The intermittent electrode darkening of section 3.2 suggests that the local turbulence can affect the convective cell formation, perhaps since the estimated $v_{E \times B}$ speed above is comparable to the poloidal turbulence speed in NSTX [23]. Time-averaged edge poloidal flows can also be comparable to $\sim 10^5 \text{ cm s}^{-1}$ in NBI-heated plasmas in NSTX [32]. Such turbulence and/or plasma flow effects have also been seen in the recent TORPEX biasing experiments [20, 21]

4.5. Electrode heating and glow

The electrode operation in these experiments was relatively successful in that there was very little arcing visible in the electrode current traces or in the camera images, even though some magnetic field lines connected the edge of the electrodes

to the surrounding grounded tiles (see section 2.1). The electrodes were coated with lithium during the run and had oxide layers after opening to air (as did all the carbon in the machine), but their conductivity during biasing in plasmas was apparently unaffected by the lithium.

The electron currents during positive biasing were in the range $\sim 10-30 \text{ A}$ at $+50-90 \text{ V}$ for $\sim 0.2-0.5 \text{ s}$, with a 50% duty cycle (e.g. figure 2), which corresponds to a time-averaged electrode surface heat flux of $\sim 100 \text{ W cm}^{-2}$. The expected rise in surface temperature rise for ATJ graphite at this heat flux is $\sim 200-300 \text{ }^{\circ}\text{C}$ over 0.5 s [33], which is well within the range of graphite operation. The electrode surface temperature was estimated from the IR emission at $\sim 0.9-1.1 \text{ nm}$ during later cycles of biasing as in figure 12(d) to be $\sim 700 \text{ }^{\circ}\text{C}$ [34]. This higher temperature may be due to a poorly thermally conducting surface layer which formed on the electrodes during operation. The electrical resistance of the electrodes (without coatings) was $\leq 0.5 \Omega$, so the resistive heating of the electrode due to the electrode current should have been negligible.

An unexpected phenomenon was the bright glow seen at the electrode surfaces in Li I light (670.8 nm) after $\sim 50-100 \text{ ms}$ of biasing, as shown in figures 4, 6, 9 and 10. This was not blackbody radiation, since no similar light was seen in the nearby D_{α} line, and since the IR emission level was $\sim 100\times$ lower. This glow was not simply due to the electron flux on lithium, since it did not appear during the first few electrode biasing cycles. Probably this Li I glow was due to enhanced evaporation of the lithium from the electrode surfaces above $\sim 400 \text{ }^{\circ}\text{C}$, and the subsequent excitation of the lithium neutral atoms just above the surface. This glow was sometimes non-uniform across the electrode surface (e.g. figure 12(d)), suggesting effects of a variable surface coating. However, there does not seem to be a substantial increase in local plasma density due to this electrode glow effect, since the electrode and probe currents do not increase proportionally to the Li I light from the electrode glow.

4.6. Conclusions and further directions

The main conclusion of this experiment is that the divertor electrodes caused some consistent changes in the local plasma when they were biased positively and were near the outer strike point. Namely, increases in the local probe currents and Li I light emission were observed at the larger major radius end of the electrodes, which turned on and off within 1 ms of the biasing. There was also evidence for a $\leq 1 \text{ cm}$ penetration of this electrode bias across the B -field to the nearby Langmuir probes. When the electrodes were farther away from the outer strike point there were only small intermittent decreases in the Li I light emission at the small major radius end of the positive electrode during biasing. These changes could be qualitatively consistent with the expected upward and downward vertical motion due to a convective cell generated by the electrodes. However, we could not provide a quantitative explanation of these effects due to the limited diagnostics and large uncertainties in the modeling.

These local biasing effects were produced only using a relatively large electrode current density ($\sim 4 \text{ A cm}^{-2}$)

and power ($\sim 200 \text{ W cm}^{-2}$), which caused the electrode temperature to increase within ~ 100 ms. Thus to control the entire divertor scrape-off layer in a steady-state tokamak, a switchable multi-electrode toroidal array of divertor plate electrodes would probably be needed. For NSTX this would require at least ~ 100 times the electrode area and power used in the present experiment, i.e. a few hundred kilowatts. Although such system would be complicated, it could in principle rapidly adjust the scrape-off layer heat flux over a few centimeters without overheating the electrodes, provided the effects of each electrode are better understood.

Clearly more work in the area of diagnostics and modeling are needed to understand the effects of electrodes in the divertor region of a tokamak. For example, the electrostatic potential changes inside the electrode flux tube need to be measured along with the potential distribution perpendicular and parallel to B . Modeling of the effect of these electrodes will need to take into account the changes produced by the electrodes on the local plasma, and so will become a strongly nonlinear problem.

Finally, we note that significant progress has very recently been made on diagnostics and modeling of the biasing experiments in TORPEX [35], but that the control of an actual tokamak scrape-off layer will ultimately need to be demonstrated in a large tokamak. Ultimately, more practical methods for large tokamaks would be to use multiple cold gas injectors at the divertor plate to create local convective cells by controlling the local plasma temperature [2], although this has not been systematically attempted yet.

Acknowledgments

We thank R Bell, R H Cohen, E Fredrickson, K Gan, J Hosea, M Jaworski, I Joseph, R Kaita, A Khodak, H Kugel, D D Ryutov, V Soukanovskii, D Stotler and G Taylor and the NSTX group for their contributions to this experiment, which was performed under USDOE Contract DE-AC02-09CH11466.

References

- [1] Loarte A *et al* 2007 *Nucl. Fusion* **47** S203
- [2] Cohen R H and Ryutov D D 1997 *Nucl. Fusion* **37** 621
- [3] Ryutov D D *et al* 2001 *Plasma Phys. Control. Fusion* **43** 1399
- [4] Cohen R H *et al* 2007 *Plasma Phys. Control. Fusion* **49** 1
- [5] Joseph I *et al* 2009 *Phys. Plasmas* **16** 052510
- [6] Strait E 1981 *Nucl. Fusion* **21** 943
- [7] Doerner R P *et al* 1994 *Nucl. Fusion* **34** 975
- [8] Kaye S M *et al* 1994 *Plasma Phys. Control. Fusion* **36** A51
- [9] Decoste R *et al* 1994 *Phys. Plasmas* **1** 1497
- [10] Schaffer M J *et al* 1996 *Nucl. Fusion* **36** 495
- [11] Hara J *et al* 1997 *J. Nucl. Mater.* **241** 338
- [12] Gravier E *et al* 2002 *Nucl. Fusion* **42** 653
- [13] van Oost G *et al* 2003 *Plasma Phys. Control. Fusion* **45** 621
- [14] Weynants R R *et al* 2005 *Fusion Sci. Technol.* **47** 202
- [15] Stockel J *et al* 2005 *Plasma Phys. Control. Fusion* **47** 635
- [16] Kitajima S *et al* 2011 *Nucl. Fusion* **51** 083029
- [17] Xu Y *et al* 2011 *Nucl. Fusion* **51** 063020
- [18] Counsell G *et al* 2003 *J. Nucl. Mater.* **313–316** 804
- [19] Zweben S J *et al* 2009 *Plasma Phys. Control. Fusion* **51** 105012
- [20] Theiler C *et al* 2011 *Phys. Plasmas* **18** 055901
- [21] Theiler C *et al* 2012 *Phys. Rev. Lett.* **108** 065005
- [22] Scotti F *et al* 2012 *Rev. Sci. Instrum.* **83** 10E532
- [23] Maqueda R J *et al* 2010 *Nucl. Fusion* **50** 075002
- [24] Jaworski M A *et al* 2012 *Fusion Eng. Des.* in press
- [25] Farina D *et al* 1993 *Nucl. Fusion* **33** 1315
- [26] Rozhansky V A *et al* 1999 *Nucl. Fusion* **39** 613
- [27] Carlson A 2001 *Phys. Plasmas* **8** 4732
- [28] Bergmann A 2002 *Phys. Plasmas* **9** 3413
- [29] Wolters U *et al* 1999 *Plasma Phys. Control. Fusion* **41** 721
- [30] Gunn J P 1997 *Phys. Plasmas* **4** 4435
- [31] Zweben S J *et al* 2006 *Phys. Plasmas* **13** 056114
- [32] Bell R *et al* 2010 *Phys. Plasmas* **17** 082507
- [33] Gan K *et al* 2012 *Rev. Sci. Instrum.* submitted
- [34] Lyons B C *et al* 2011 *Princeton Plasma Physics Laboratory Report PPPL-4612*
- [35] Theiler C *et al* 2012 *Phys. Plasmas* **19** 082305